

High Open Circuit Voltages in *pin*-Type Perovskite Solar Cells through Strontium Addition

Pietro Caprioglio ^{*†}, Fengshuo Zu ^{‡*}, Christian M. Wolff ^{*}, José A. Márquez Prieto[‡], Martin Stolterfoht ^{*}, Pascal Becker[‡], Norbert Koch ^{‡‡}, Thomas Unold[‡], Bernd Rech [§], Steve Albrecht ^{†§} and Dieter Neher ^{*}

^{*} University of Potsdam, Institut für Physik und Astronomie, Potsdam, Germany

[‡] Humboldt-Universität, Institut für Physik, Berlin, Germany

[§] Helmholtz-Zentrum Berlin, Institute for Silicon Photovoltaics, Berlin, Germany

[†]Helmholtz-Zentrum Berlin, Young Investigator Group Perovskite Tandem Solar Cells, Berlin, Germany

[‡]Helmholtz-Zentrum Berlin für Materialien und Energie GmbH, Berlin, Germany

Supporting Information

- 1) Current density – voltage characteristic
- 2) EQE and Absorption Measurement
- 3) Radiative Losses
- 4) SIMS (Secondary Ion Mass Spectroscopy)
- 5) XPS (X-Ray Photoelectron Spectroscopy)
- 6) SEM (Scanning Electron Microscopy)
- 7) Recombination Dynamic Simulations
- 8) Surface Photovoltage Effect
- 9) Photoemission Spectroscopy
- 10) Photoluminescence Quantum Yield

1. Current density – voltage characteristic

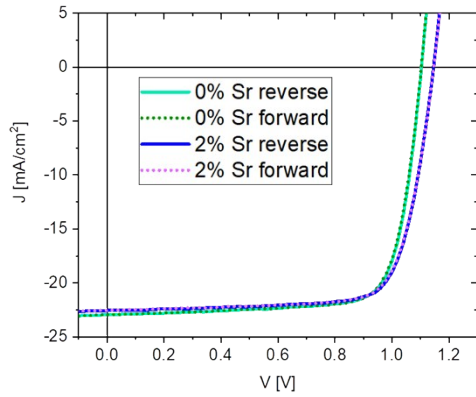


Figure SIA: J-V characteristic showing both forward and reverse scan at 0.1V/s with a voltage step of 0.02 V for two samples containing 0% and 2% Sr respectively. Both samples show complete absence of any hysteresis effect.

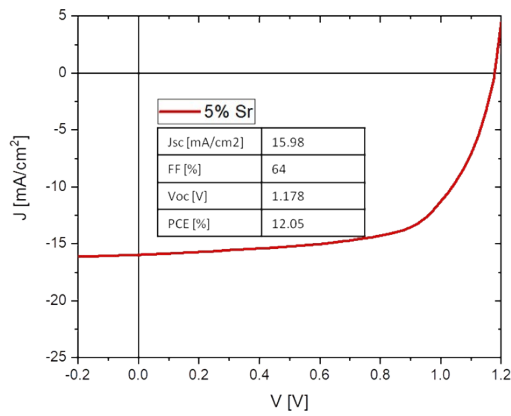


Figure SIB: J-V characteristic showing a reverse scan at 0.1V/s with a voltage step of 0.02 V for a sample containing 5% Sr. The curve shows how a higher Sr concentration has negative effects on both J_{sc} and FF without any appreciable improvement of the V_{oc} .

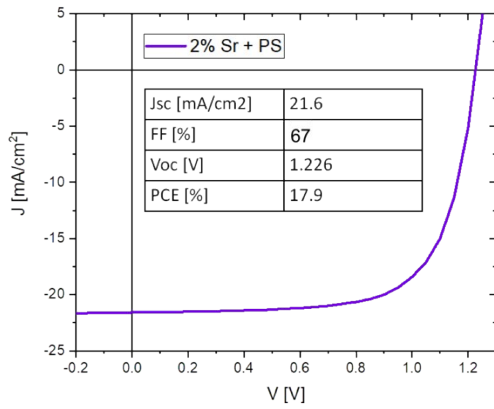


Figure S1C: *J-V* characteristic showing a reverse scan at 0.1V/s with a voltage step of 0.02 V for a sample containing 2% Sr with additional ultra-thin (less than 5nm) polystyrene layer deposited between perovskite and C_{60} following the experimental procedure described in Wolff et al.¹ The resulting solar cell show an extraordinarily high V_{oc} of 1.215V. Unfortunately, the presence of this insulating PS layer led to a considerable reduction of the FF, probably by limiting the extraction of charges via tunneling¹

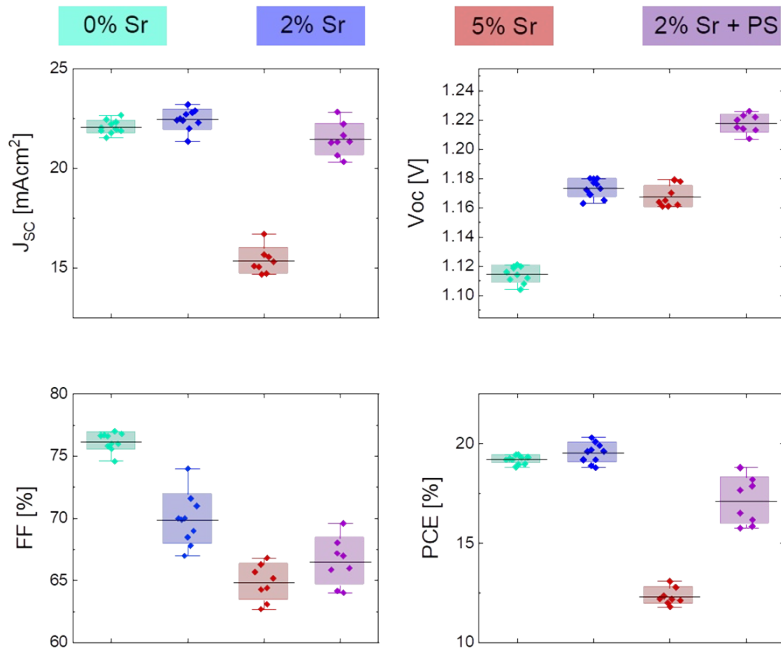


Figure S1D: Box chart for the most relevant type of devices, 0% Sr, 2% Sr, 5% Sr and 2%Sr + PS. From the picture trends are more evident: it is clear that upon Sr addition the V_{oc} is improved whereas

the FF decreases. We can identify a ratio of 2% Sr as the optimum concentration considering the strong decrease in performances observed with a 5% Sr ratio, without showing any further improvement in V_{oc} . On the contrary, the addition of a polystyrene layer onto a 2% Sr increase considerably further the V_{oc} reaching a record value of 1.226 V. However, it is also clear of this has a negative effect on the FF and the overall PCE unfortunately is not improved. For this reason we refer to this additional increase in V_{oc} as a proof of concept for the suppression of recombination at the interface with C_{60} .

2. EQE and Absorption Measurement

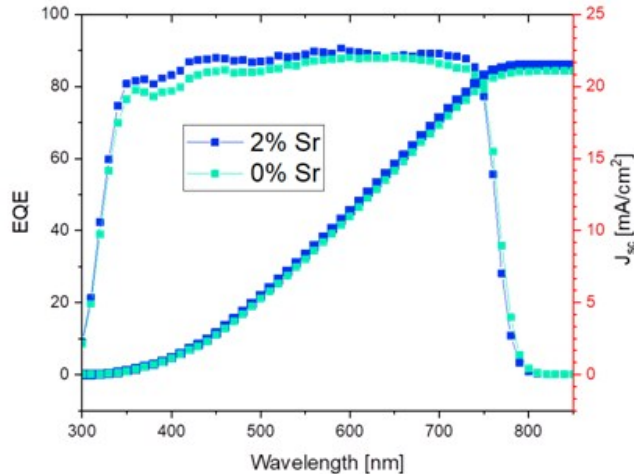


Figure S2A: External Quantum Efficiency including the integrated current for 0% and 2% Sr cells. We acknowledge that for the 2% Sr cell the integrated current of 21.5 mA/cm² represents approximately a 4% relative mismatch compared to the J_{sc} of 22.4 mA/cm² as obtained from the JV scan of the corresponding solar cell. A similar mismatch has been systematically found for the 0% Sr cell.

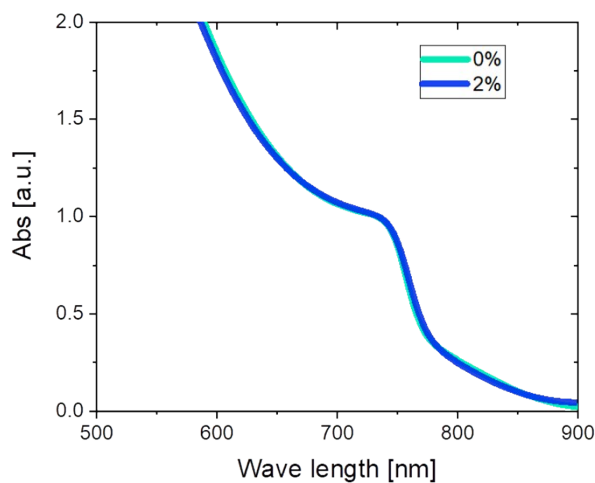


Figure S2B: Absorption measurement of two perovskite film with same thickness (400nm) with 0% and 2% Sr respectively, deposited on glass.

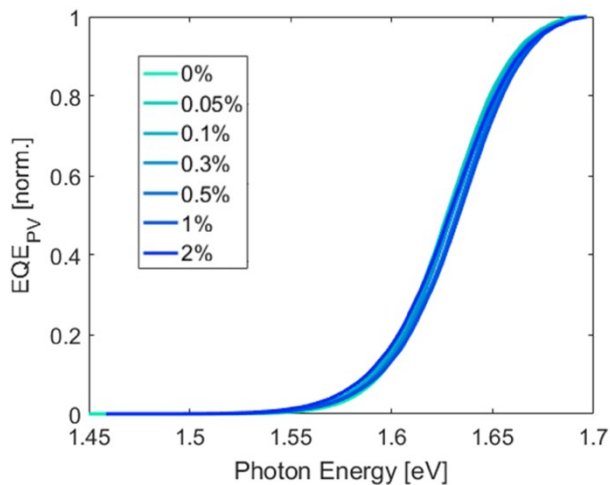


Figure S2C: EQE_{PV} onset as function of photon energy for all different Sr concentrations, normalized to 1.7 eV.

3. Radiative losses

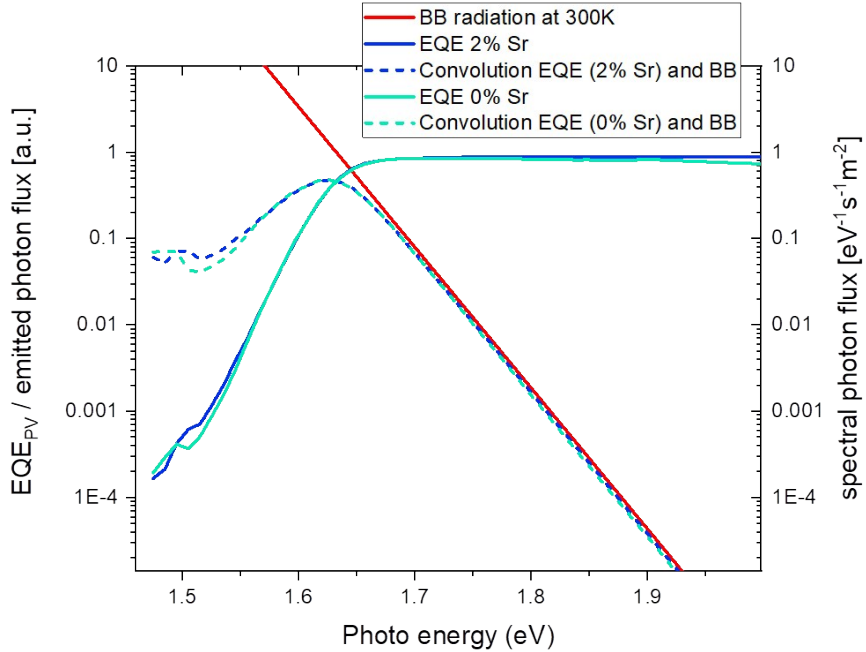


Figure S3: EQE_{PV} onset of two perovskite solar cell containing 0% and 2% Sr respectively and their emitted spectral photon flux calculated when the device is in equilibrium with the black-body (BB) radiation of the surroundings at 300K according to equation S1.

Approach used in Fig. S6 follows the report by Rau et al.². Briefly the Black Body photon flux is

$$\phi_{BB} = \frac{1}{4\pi^2 \hbar^3 c^2} \frac{E^2}{\exp\left(\frac{E}{k_B T}\right) - 1} \quad (S1)$$

with \hbar Plank's constant, k_B Boltzmann constant and T temperature. Assuming that the perovskite solar cell is at 300K in thermal equilibrium with its environment, the dark radiative recombination current is:

$$J_{em,0} = e \int EQE_{PV}(E) \phi_{BB}(E) dE = J_{rad,0} \quad (S2)$$

with EQE_{PV} the photovoltaic external quantum efficiency of the perovskite solar cell and $J_{em,0}$ the current giving rise to emission, which also defines the dark radiative recombination current at $V = 0$.

From that, the radiative $V_{oc,rad}$ ($EQE_{EL} = 1$) can be calculated with the following equation:

$$V_{oc,rad} = \frac{k_B T}{e} \ln \left(\frac{J_G}{J_{rad,0}} + 1 \right) \quad (\text{S3})$$

where J_G is the generation current under illumination, in this case approximated to the short circuit current J_{sc} .

For a more detailed derivation refer to Ref. 2.

4. SIMS (Secondary Ion Mass Spectroscopy)

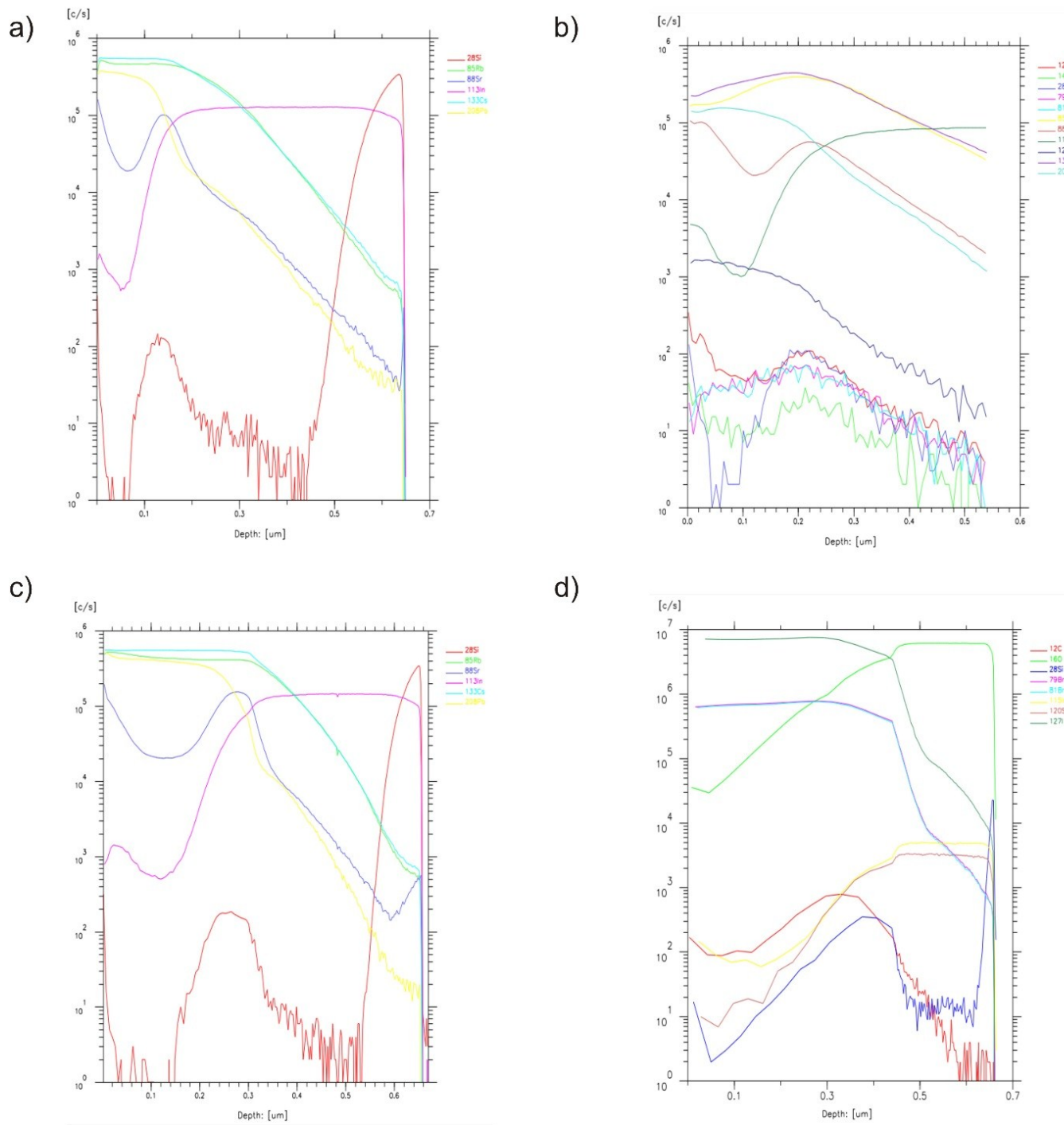


Figure S4: a) and b) SIMS (Secondary Ion Mass Spectroscopy) depth profile of two different spots on the surface of the same perovskite sample containing 2% Sr. c) SIMS depth profile of the different perovskite sample containing 2% Sr. All measurements here are performed using O ions. d) SIMS depth profile using Cs ions in order to detect the distribution of Br and I across the perovskite layer.

5. XPS (X-Ray Photoelectron Spectroscopy)

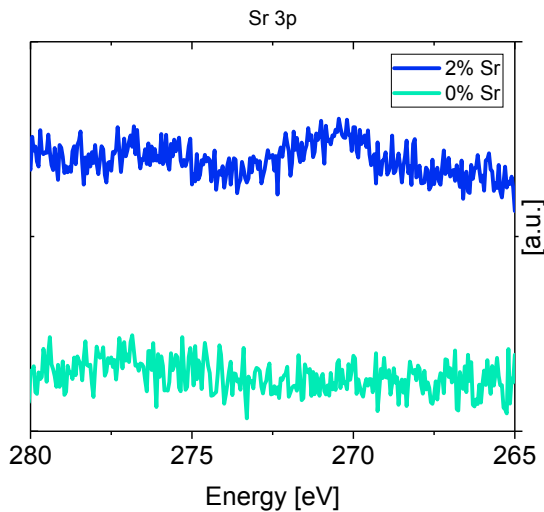


Figure S5A: XPS measurements of the surface of two perovskite layers containing 0% and 2% Sr respectively.

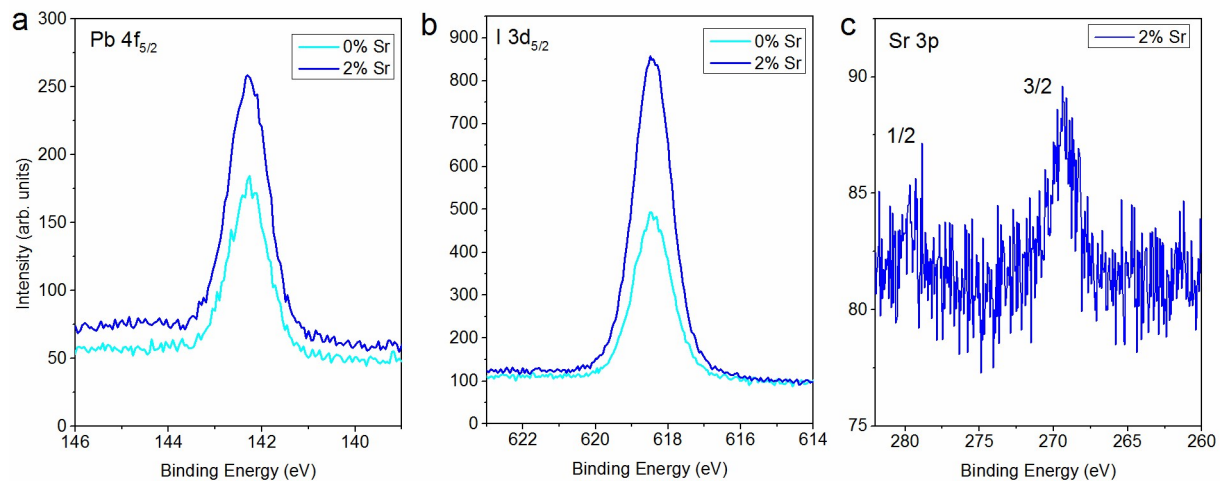


Figure S5B: XPS core-level spectra of (a) Pb 4f, (b) I 3d and (c) Sr 3p on two mixed perovskite films without and with 2% Sr incorporation.

In order to investigate quantitatively the surface composition of the perovskite films, XPS measurements employing monochromated Al $\text{k}\alpha$ radiation were performed on the samples without and with Sr incorporation. As shown in Figure S5, clearly, we observed relatively large amount of Sr on the perovskite surface with 2% Sr. Detailed analysis of the core-level spectra results in the Sr/Pb molar ratio of 0.21 and the Sr/I molar ratio of 0.07, which are both much higher than the expected

stoichiometry from an homogenous Pb substitution through the whole volume. This proves strong enrichment of Sr on the perovskite surface, in good agreement with the findings by Perez Del Rey et al.³. Moreover, if the surface would be covered with unreacted SrI_2 the I concentration found at the surface, and consequently its ratio with Sr, should be consistently higher than what found here. In addition, the I/Pb molar ratio (2.49 by stoichiometry) is estimated to be 2.78 for the sample with Sr, in contrast to 2.13 for the sample without Sr, which can be possibly ascribed to the fact that Sr partially replace Pb, leading to a decrease of Pb/I ratio at the surface in the crystal lattice.

6. SEM (Scanning Electron Microscopy)

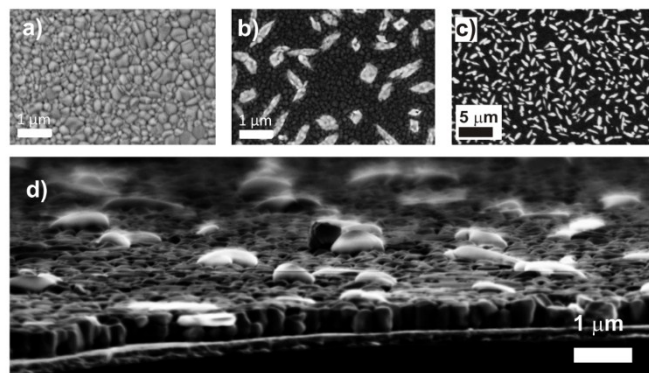


Figure 6A: Energy sensitive SEM in-lens detector top view images of perovskite films with a) 0% Sr and b) 2% Sr. c) shows a zoomed-out view of the same sample as in b). Image d) displays SEM in-lens detector images of a tilted sample containing 2% of Sr to visualize the cross section.

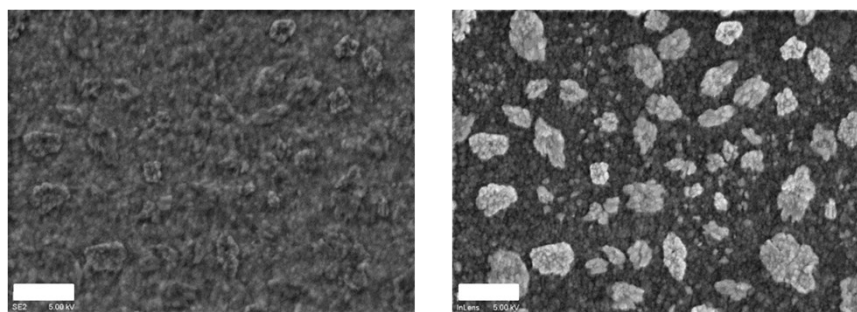


Figure S6B: Comparison between Everhart-Thornley detector (left) and In-Lens detector (right) imaging of a 2% Sr sample. The images show that the brighter feature on the top surface can be

imaged only through the energy sensitive In-Lens detector whereas with the more topographic sensitive detectors those are barely visible. The comparison shows how from a more topography sensitive imaging it is possible to barely distinguish these features only by a light shadowing effect due to the different height compared to the rest of the layer, but no change in brightness is observed, excluding the presence of non-conductive material. Scale bar here is $1 \mu\text{m}$.

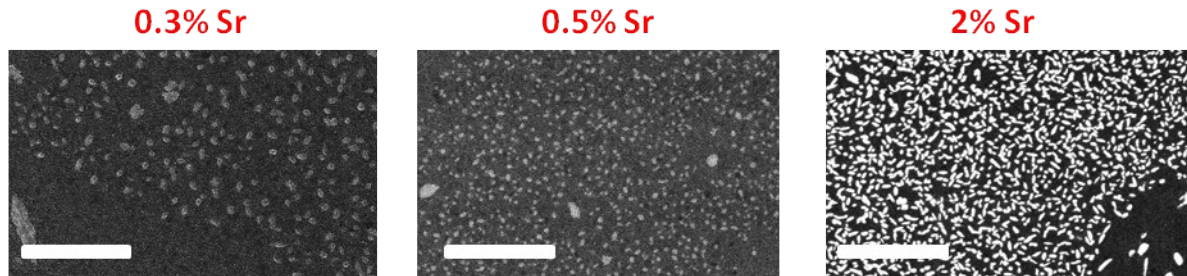


Figure S6C: Top SEM images of 0.3%, 0.5% and 2% Sr samples. The series of images indicates that increasing the Sr concentration the density of the brighter feature on top increase. Scale bar here is $10 \mu\text{m}$.

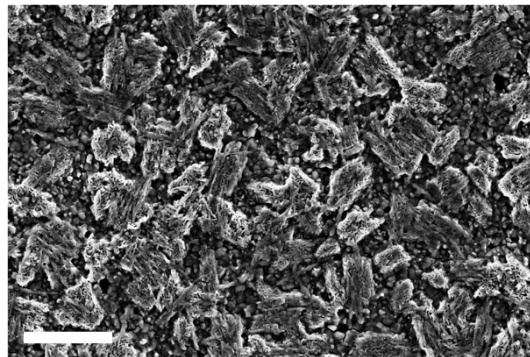


Figure S6D: Top SEM images of a 5% Sr sample. The image indicates that increasing the Sr concentration the density of the brighter feature on top increase. As expected, in this case the surface is almost entirely covered with feature of a different nature from the underlying perovskite typical paddlestones. This, consistently with the reduced PCE, indicates that in this case amount of Sr added is probably too much and that the elevated concentration of this features, beneficial in the case of 2%, now could substantially limits the performance of the resulting solar cell. Scale bar here is $2 \mu\text{m}$.

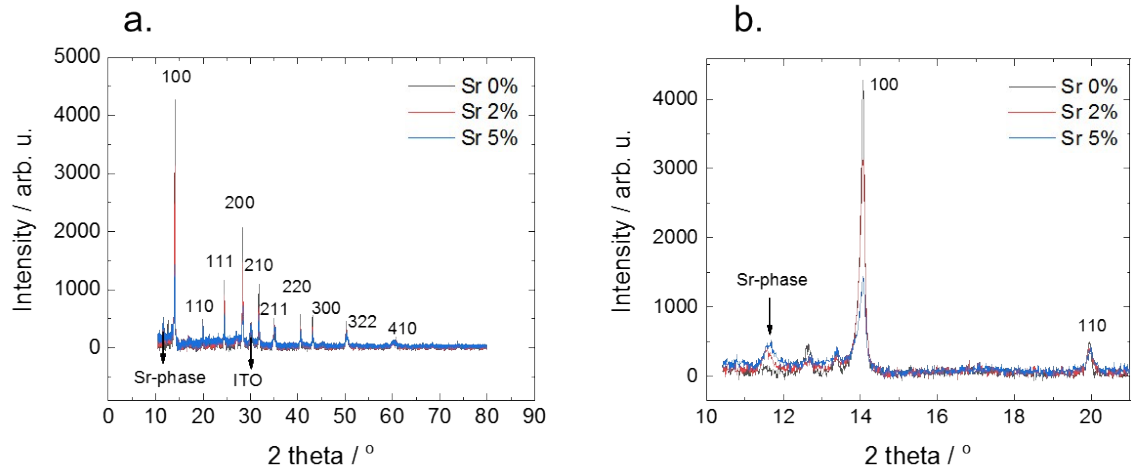


Figure S6E: a) X-ray diffraction patterns for samples containing 0%, 2% and 5% Sr respectively. The patterns show the typical perovskite distinctive peaks for all three samples (space group Pm-3m). No significant shifts are observed in the reflections of the perovskite phase indicating no major changes in the unit cell volume. b) Magnification of X-ray diffraction patterns for samples containing 0%, 2% and 5% Sr respectively. Concomitantly with the presence of Sr in the films, at $\sim 11.6^\circ$ a new reflection not identified in the 0% Sr sample appears. Since this is the only new reflection appearing, the exact identification of the crystal structure and the chemical nature of this phase is rather difficult, particularly taking into account the chemical complexity of the films. More importantly, the intensity of the perovskite reflections decrease as the new phase appears. This potentially indicates that the new phase segregates towards the surface of the film attenuating the X-ray signals coming from the underlying perovskite phase. We additionally note that the broadening of the peaks increase as the Sr content increases in the sample. This might be caused by an increase in microstrain and/or reduction of the domain size. An increase of microstrain might be caused by an increase of point or planar defect concentration or a decrease of the compositional uniformity of the domains.

7. Recombination Dynamic Simulations

In this simulation the recombination of charges has been simulated using the following rate equation

$$\frac{dn}{dt} = - (k_1 n + k_2(n_0 + n) \cdot n + k_3 n^3) \quad (S4)$$

where n is the initial photogenerated carrier density, n_0 is the background carrier concentration due to doping, and k_1 , k_2 and k_3 are the monomolecular, bimolecular and Auger recombination coefficient, respectively. The simulations were carried out in MATLAB R2017b, running an iterative code with the given constants and equations. To obtain the steady state carrier concentration we assumed $G = 4 * 10^{21} \text{ cm}^{-3}\text{s}^{-1}$ and let the time run for ~ 10 ms until steady state conditions were assured.

Figure S7A displays the result of simulations where the background carrier concentration n_0 was varied. For the pulsed simulation we assumed $n_{t=0} = 1 * 10^{14} \text{ cm}^{-3}$ at $t = 0$ and no further generation thereafter. In this case we simulated the recombination dynamic varying the doping concentration n_0 from $n_0 = 1 * 10^{14} \text{ cm}^{-3}$ to $n_0 = 1 * 10^{18} \text{ cm}^{-3}$, whereas the recombination constants fixed at $k_1 = 4 * 10^6 \text{ s}^{-1}$, $k_2 = 1 * 10^{-10} \text{ s}^{-1}$ and $k_3 = 1.8 * 10^{-28} \text{ s}^{-1}$, being those realistic values and similarly already reported in literature^{4,5}. The PL efficiencies at a carrier concentration equivalent to 1 sun has been simulated using

$$PL = k_2 \cdot (n + n_0) \cdot n \quad (S5)$$

and

$$PLQY = \frac{k_2 \cdot (n + n_0) \cdot n}{(k_1 n + k_2(n_0 + n) \cdot n + k_3 n^3)} \quad (S6)$$

The simulations show that increasing the background density due to doping provides additional centres for radiative recombination (we assumed exclusively radiative second order recombination), with the effect of increasing the radiative efficiency but at the same time enhancing the speed of the recombination of photogenerated charges, resulting in faster PL decays. Clearly, a very different situation is found in our study when increasing the Sr concentration, where we observe a parallel increase of the PL life times and PL efficiencies.

To explain the experimental results, a second set of simulations were performed where the PL decay rate and absolute PL efficiency was simulated for different k_1 in absence of doping. In this case simulation shows how the reduction of k_1 has positive effects on both PL decays and efficiencies.

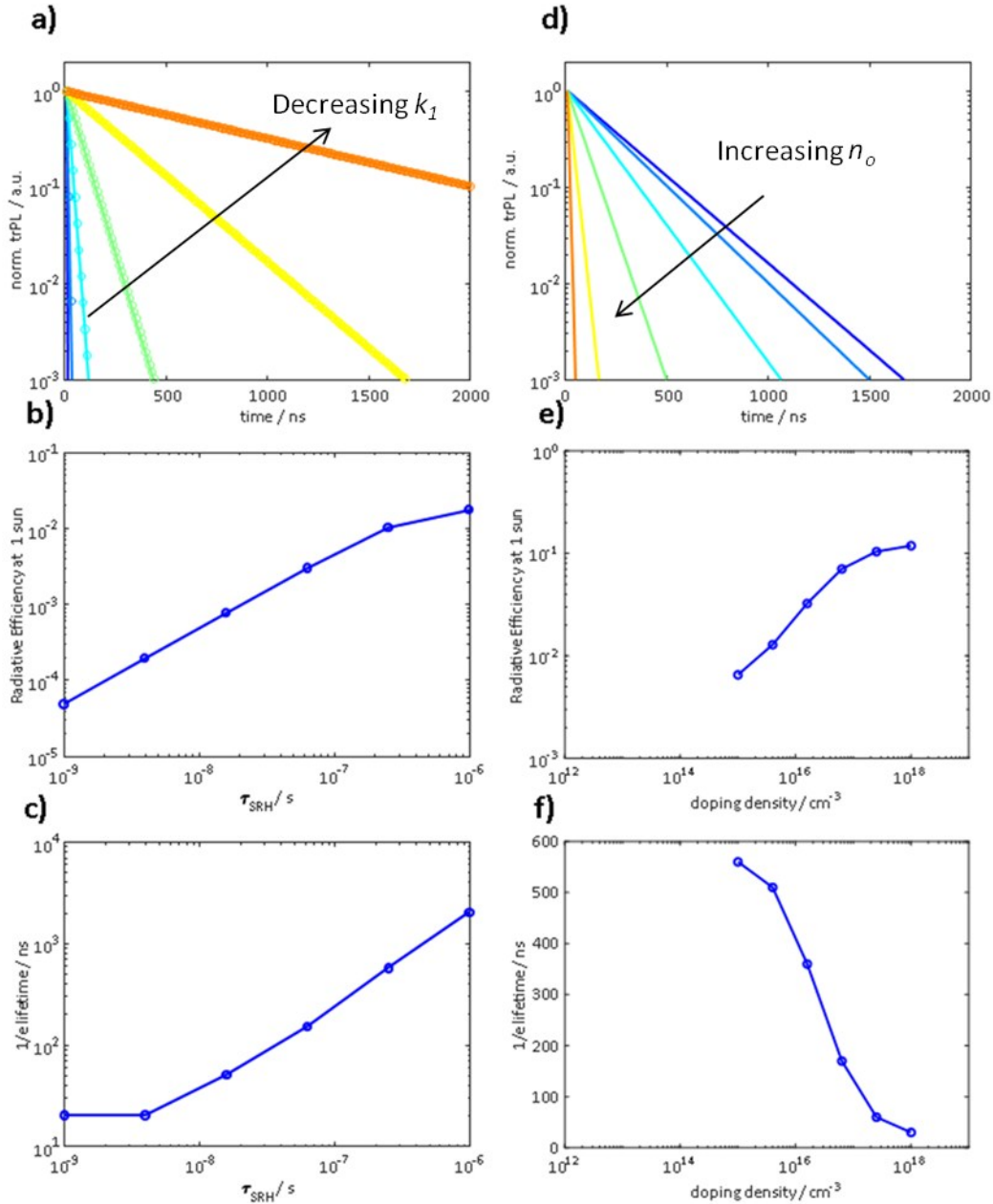


*Figure S7A: Simulations of photoluminescence decays at low intensities ($n_{t=0} = 10^{14} \text{ cm}^{-3}$), a) and d), radiative efficiencies (PLQY), b) and e), and $1/e$ PL decay, c) and f). On the left side, a), b) and c), the simulations present the results for reducing the monomolecular rate constant k_1 from 10^0 and 10^6 s^{-1} and plotted against the SRH life times $\tau_{SRH} = 1/k_1$. On the right side, d), e) and f), we increase the background doping concentration from 10^{15} to 10^{18} cm^{-3} , using a fixed $k_1 = 4 * 10^6 \text{ s}^{-1}$.*

8. Surface Photovoltage Effect (measured by UPS)

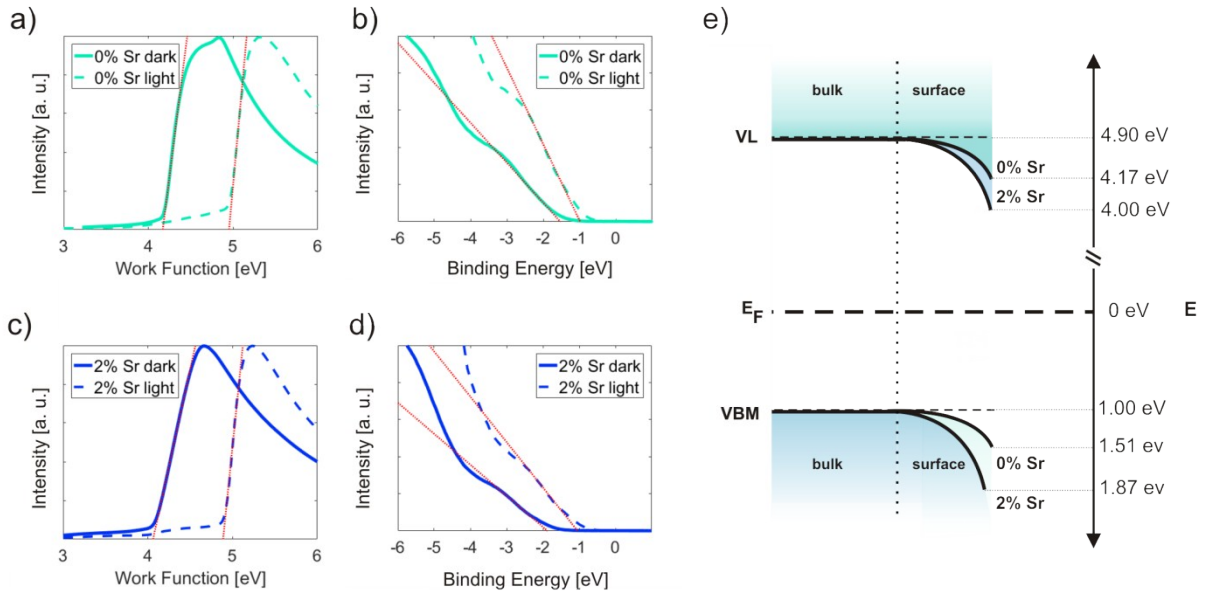


Figure S8: Effect of visible light illumination on the work function and valence band for 0% Sr and 2% Sr containing samples. a) and c) work function measured under dark and illumination conditions. b) and d) valence band regions measured under dark and illumination conditions. e) schematic representation of the surface band bending for 0% and 2% Sr-perovskites in the dark and under illumination. Vacuum level (VL) and valence band maximum (VBM) positions are given with respect to the Fermi level of the substrate (E_F).

9. Photoemission Spectroscopy

While we refrained from measurements of intermediate C_{60} coverage to minimize eventual sample changes due to prolonged illumination with UV light, we can yet draw a realistic picture of the energy level alignment based on prior art, as follows. Since the electron affinity of C_{60} is in the range of 4.0 eV⁶ to 4.9 eV (our measurements, Fig. S9A in the SI), contact with a substrate of comparable work function will result in Fermi level pinning, i.e., electron transfer from the substrate to the acceptor C_{60} and thus partial filling of its LUMO manifold⁷. In our case the substrate is the perovskite film, and the

electron transfer to the molecular layer will result in reduced downward surface band bending within the perovskite⁸. The accumulated electron density with the C₆₀ layer promotes charge carrier diffusion away from the interface, i.e., upward energy level bending within the acceptor layer occurs^{7,9}, in full analogy to band bending in conventional semiconductors. Note that the amount of energy level bending, as well as final work function and Fermi level position within the energy gap of the acceptor depend on the amount of transferred charge and details of the actual density of states distribution⁹, which can be notably influenced by structural disorder. In addition, we stress that the Fermi level position of a 20 nm thick C₆₀ layer is still determined by the substrate and does not represent the intrinsic position, as the Debye length of C₆₀ was reported to be several 100 nm¹⁰. Consequently, there are three components that contribute to the work function of the 20 nm C₆₀ layer, i.e., reduced downward surface band bending within the perovskite, an interface dipole due to the transferred charge, and upward energy level bending within the C₆₀ film. Attending to the two specific examples examined here, we first observe that the work function of 0% Sr perovskites was consistently 0.15 eV (or more) higher than that of 2% Sr samples, and thus a larger amount of electron transfer to the C₆₀ layer when Sr is incorporated into the perovskite. This implies stronger energy level bending within the C₆₀ and indeed justifies the observation of higher work function, as well as wider energy spacing between Fermi level and LUMO for the C₆₀/2% Sr perovskite interface, compare to the Sr-free one.

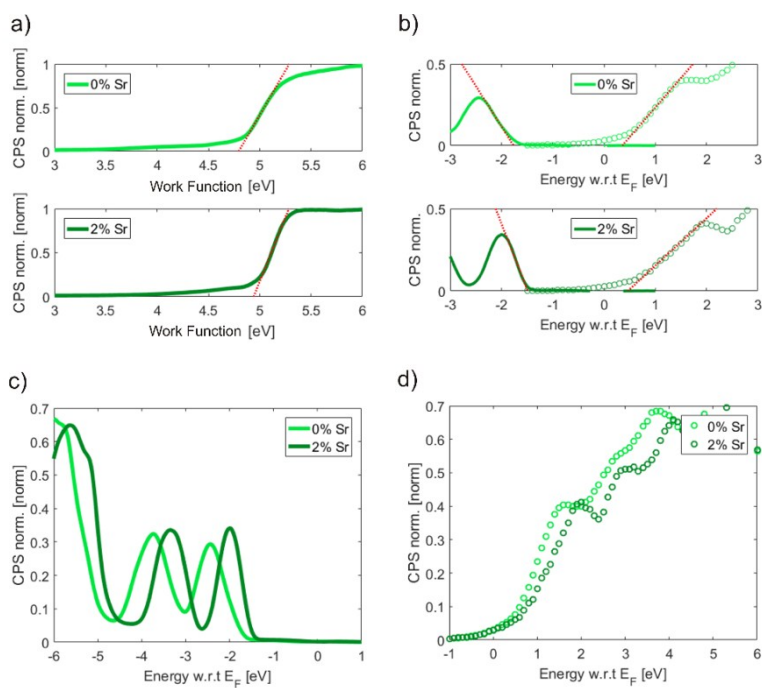


Figure S9A: UPS and IPES data of 20nm layer C₆₀ deposited on two different ITO/PTAA/perovskite samples, containing 0% and 2% Sr respectively. a) Secondary electron cut-off regions. b) Magnified valence and conduction band region near E_F. c) Wide range of valence band structure obtained from UPS and d) conduction band structure obtained from IPES.

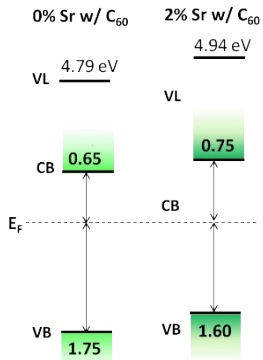


Figure S9B: Valance band maximum, conduction band minimum and work function energy scheme using values extrapolated from UPS/IPES (Fig. S9A) for two layers of 20nm C₆₀ deposited on two different PTAA/perovskite samples, containing 0% and 2% Sr respectively.

10. Photoluminescence Quantum Yield at Perovskite/C₆₀ interface.

To study the importance of non-radiative recombination at the perovskite/C₆₀ interface, different samples with and w/o a 30 nm thick C₆₀ layer were subject to absolute PL measurements. This new set of measurements has been performed using a 445nm CW laser (adjusted ad 1 sun condition intensity) exciting our sample through an optical fiber connected to an integrating sphere. The PL spectra have been recorded with a Silicon CCD camera (Andor), calibrated with a Xe lamp of know spectral irradiance. The spectral photon density has been obtained from the corrected detector signal and the photon numbers of the excitation and emission obtained from numerical integration carried out in MATLAB R2017b. The PLQY values in Fig. S10 confirm how indeed the presence of C₆₀ drastically reduces the PL efficiency compared to the neat perovskite layer. The measurements also show that this

reduction is significantly smaller for the Sr-containing perovskite, meaning that non-radiative recombination at this “unfavourable” interface has been reduced. This finding is perfectly in agreement with the increase in V_{oc} observed in the device and the recombination scheme proposed for the Sr-containing samples, where the selectivity of the contact is improved due to the present of a larger bandgap and strong downward band bending, which limits the accessibility of holes to this interface. We acknowledge that the PL values measured for this new set of experiments during resubmission period are overall slightly lower than what we should expect from the high V_{oc} of our devices, most probably due to the present unfavourable conditions of our gloveboxes which has affected sample preparation during resubmission period (most probably caused by the exceptionally elevated temperature and high degree of humidity recorded during this period of the year in Germany).

However, the trend our results is solid and clear for multiple sets of samples.

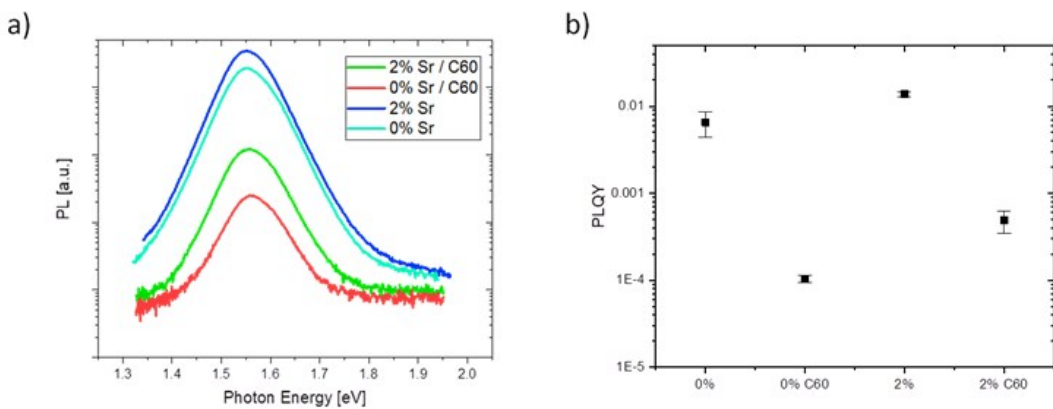


Figure S10: a) Photoluminescence Quantum Yield (PLQY) measurements for a neat 0% and 2% Sr sample and covered with 30nm of C₆₀. Averaged PLQY values, b), for the corresponding set of samples. Statistics here is calculated over 4 films for each type of sample.

Bibliography

- 1 C. M. Wolff, F. Zu, A. Paulke, L. P. Toro, N. Koch and D. Neher, *Adv. Mater.*, 2017, **29**, 1700159.
- 2 U. Rau, *Phys. Rev. B*, 2007, **76**, 85303.
- 3 D. Perez-del-Rey, D. Forgacs, E. M. Hutter, T. J. Savenije, D. Nordlund, P. Schulz, J. J. Berry, M. Sessolo and H. J. Bolink, *Adv. Mater.*, 2016, **28**, 9839–9845.
- 4 M. B. Johnston and L. M. Herz, *Acc. Chem. Res.*, 2016, **49**, 146–154.
- 5 J. M. Richter, M. Abdi-Jalebi, A. Sadhanala, M. Tabachnyk, J. P. H. Rivett, L. M. Pazos-Outón, K. C. Gödel, M. Price, F. Deschler and R. H. Friend, *Nat. Commun.*, 2016, **7**, 13941.
- 6 J. Hwang, A. Wan and A. Kahn, *Mater. Sci. Eng. R Reports*, 2009, **64**, 1–31.
- 7 H. Wang, P. Amsalem, G. Heimel, I. Salzmann, N. Koch and M. Oehzelt, *Adv. Mater.*, 2014, **26**, 925–930.

- 8 R. Schlesinger, Y. Xu, O. T. Hofmann, S. Winkler, J. Frisch, J. Niederhausen, A. Vollmer, S.
Blumstengel, F. Henneberger, P. Rinke, M. Scheffler and N. Koch, *Phys. Rev. B*, ,
DOI:10.1103/PhysRevB.87.155311.
- 9 M. Oehzelt, N. Koch and G. Heimel, *Nat. Commun.*, , DOI:10.1038/ncomms5174.
- 10 H. Ishii, N. Hayashi, E. Ito, Y. Washizu, K. Sugi, Y. Kimura, M. Niwano, Y. Ouchi and K.
Seki, *Phys. Status Solidi Appl. Res.*, 2004, **201**, 1075–1094.